

Non-linear Monte Carlo Ray Tracing for Visualizing Warped Spacetime

Avirup Mandal^{1a}, Kumar Ayush^{1a} and Parag Chaudhuri¹

¹*Indian Institute of Technology Bombay, Powai, Mumbai, India*

{mandal.avirup, cheekujodhpur}@gmail.com, paragc@cse.iitb.ac.in

Keywords: Raytracing, Non-linear Monte Carlo, Warped Spacetime, Relativity.

Abstract: General relativity describes the curvature of spacetime. Rays of light follow geodesic paths in curved spacetime. Visualizing scenes containing spacetime regions with pronounced curvature requires tracing of these light ray paths. We present a Monte Carlo approach for non-linear raytracing to render scenes in curved spacetime. In contrast to earlier work, we can accurately resolve ray-object interactions. This allows us to create plausible visualizations of what happens when a black hole appears in a more known environment, like a room with regular specular and diffuse surfaces. We demonstrate that our solution is correct at cosmological scales by showing how spacetime warps around a stationary Schwarzschild black hole and a non-stationary Kerr black hole. We verify that the solution is consistent with the predictions of general relativity. In the absence of any curvature in spacetime, our renderer behaves like a normal linear ray tracer. Our method has the potential to create rich, physically plausible visualizations of complex phenomena that can be used for a range of purposes, from creating visual effects to making pedagogical aids to understand the behaviour of spacetime as predicted by general relativity.

1 INTRODUCTION

General relativity changed the way in which we understand our universe. The theory presented by Einstein in 1915 has been verified via multiple experimental observations. However, the concept of curved spacetime that is central to this theory stays elusive to a casual reader. Even students of physics have trouble visualizing what curved spacetime looks like because it is so far removed from our daily experience. It was only recently that a visualization of curved spacetime was created that is true as per general relativity and it depicted how a black hole would look to an observer much closer to it (James et al., 2015a) (James et al., 2015b). The cosmological phenomenon visualized in these works were a rotating black hole and a wormhole.

A black hole can be described as a region in space where the gravitational field is so strong that no matter or radiation can escape. The boundary of the region from which no escape is possible is called the event horizon. According to the general theory of relativity, a body of sufficient mass can deform or warp spacetime around it and result in a black hole. A static black hole, which possesses no electric charge or angular

momentum is referred to as a Schwarzschild black hole (Schwarzschild, 1916). A Kerr black hole (Kerr, 1963) on the other hand, possesses angular momentum and rotates. Another related cosmological phenomenon is a wormhole, which is like a hole punched through curved spacetime connecting two different regions of spacetime. An example of this is the Ellis Wormhole, visualized in the movie Interstellar (Ellis, 1973) (Morris and Thorne, 1988) (Thorne, 2015).

The curving of spacetime, however, is a fact predicted by the theory of general relativity and is present in the vicinity of any object that has mass. We are interested in visualizing not only black holes, but any warped spacetime, both at cosmological and at earth-like or everyday scales. We present in this paper a ray tracing method that allows us to visualize any arbitrary scene in any type of spacetime. We can stochastically trace rays in the warped spacetime, while taking care of normal light-surface interactions like reflection and refraction. This allows us to visualize everyday geometry in strongly curved spacetimes. We believe our work is first of its kind in being able to create such visualizations. We find the images that our renderer produces to be extremely useful in understanding the concept of curved spacetime and visualizing how the universe behaves in the presence of gravity. We also believe it is unique in being able to

^aA. Mandal and K. Ayush contributed equally to this work.

create physics-based visualizations that are of interest to generating special effects in cinema and as such, it is intended to work as a proof of concept that ray tracing in curved spacetime can easily be integrated into existing production pipelines. As a result, now we may have more realistic wormholes opening up in an alley in New York, which acts as a pathway for aliens. The major contributions of our work are listed as below

- We perform secondary ray tracing and resolve all object-ray intersections in curved space-time.
- We render our scene using complete global illuminations in warped spacetime which is essential to produce visual phenomena like soft shadows and caustics.
- We develop a non-linear ray tracing algorithm that works both in cosmological as well as terrestrial scale.

We talk about relevant current literature in the next section. We explain light paths in curved spacetime, and derive expressions for the geodesics that represent the light paths in Section 3. We present particular solutions for the Schwarzschild and Kerr metrics for non-rotating and rotating black holes respectively, and for the Ellis metric for wormholes. Then we present our simple ray integrator in Section 4. Detailed results and discussions of the results are presented in Section 5.

2 RELATED WORK

Astrophysical ray tracers have a long history. These visualizations have become adept at simulating and visualizing increasingly complex cosmological phenomena. Gas, dust and other stellar debris that has come close to a black hole but not quite fallen into it, forms a flattened band of spinning matter around the event horizon called the accretion disk. Thin accretion disks around black holes were visualized in early work in the area (Luminet, 1979). Subsequent works added color (Fukue and Yokoyama, 1988), handled rotating black holes and thicker accretion disks (Viergutz, 1993) and finally images produced by a simulated camera flyby near the disk (Marck, 1996). The special relativistic visualization of 4D space (Müller et al., 2010) and visualization of circular motion around Schwarzschild black hole (Müller and Boblest, 2011) have been explored before. The general relativistic ray tracer GYOTO (Vincent et al., 2011) uses the Hamiltonian formalism to integrate the rays backward in time. They also compute the

specific intensity that reaches the observer by integrating the radiative transfer equation along the computed geodesic. However, they assume the objects to be emissive, as most astrophysical objects of interest in such extreme environments are, and do not handle reflection and refraction from those objects, specular or diffuse. Another work presented by Müller (Müller, 2014) uses the *Motion4D* library to handle spacetime metrics and ray tracing. The GPU accelerated renderer presented in GRay (Chan et al., 2013) (Kuchelmeister et al., 2012) further parallelizes the work presented in earlier literature, to increase the throughput at which rays can be traced. Another GPU based renderer (Weiskopf et al., 2004) discusses refraction through a continuous medium of varying refractive index as an example on non-linear ray tracing, but does not tackle refraction within a warped spacetime itself.

Among other work, is also the Black Hole Flight Simulator (BHFS) (Hamilton, 2008), that shows how it looks like to travel towards and through various kinds of black holes. A ray tracing algorithm for visualizing two different spinning celestial objects, a neutron star and a quasi-Kerr black hole are described in (Psaltis and Johannsen, 2012) and (Bauböck et al., 2012) respectively.

It was only recently that visualizations with an observer placed closer to the black hole were produced. The Double Negative Gravitational Renderer (DNGR) was used to produce the imagery for the acclaimed movie Interstellar (Thorne, 2015) (James et al., 2015a) (James et al., 2015b). The renderer is unique in that it not only solves the equations for a ray-bundle propagation near a spinning black hole, but also produces extremely high resolution imagery required for a cinema production. This is done by mapping the celestial sphere around a black hole or a wormhole to the local sky of the observing camera, while accounting for the change in the cross-section of the light beam and, color and intensity changes due to Doppler shifts that occur in the process.

2.1 Comparison to state of the art

We do not claim to present any new astrophysics insights in our paper, nor do we claim to be better than DNGR in all respects. We certainly do not produce cinematic production quality images. However, we believe that to the best of our knowledge, we present the only renderer of its kind that can visualize highly warped spacetime, both in outer space and in everyday human-scale scenes like rooms and buildings. None of the previous works (Müller, 2014), (Kuchelmeister et al., 2012), (James et al.,

2015a), (James et al., 2015b) deal with simulating complete global illumination in curved spacetime.

In contrast, we can perform secondary ray tracing and accurately resolve ray-object intersection in curved spacetime. This allows us to perform global illumination and render complex scenes that consist of specular and diffuse surfaces. Thus unlike previous works, we can generate soft shadows, caustics etc in curved spacetime. Moreover, we use bidirectional ray tracing for the regions where less number of primary rays reach and perform local smoothing for regions with high numerical error. Prior work like (Müller et al., 2010) and (Müller and Boblest, 2011) deal with non-linear raytracing in a restrictive class of spacetime. Our method can handle any spacetime topology.

Visualizing the warping of spacetime around familiar geometries that represent our everyday experiences provides an unique perspective from which to understand curved spacetime, which leads us to claim that our renderer has unique pedagogical value for the casual science enthusiast who wants to understand general relativity, and to teachers and students of the subject. It is also of immense use to CGI professionals who have to architect such spacetimes for special effects in their productions, while staying true to its physics underpinnings.

3 LIGHT PATHS IN CURVED SPACETIME

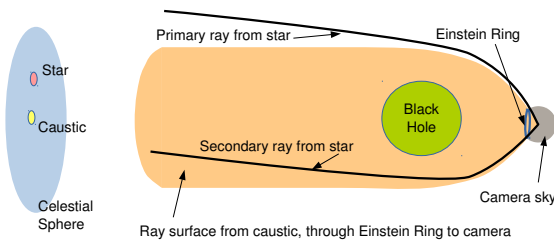


Figure 1: Schematic diagram showing the bending of light rays around a black hole.

Here we present the underlying theory behind deriving the light paths in curved spacetime, as dictated by general relativity. In layman terms, all objects with mass bend spacetime with the curvature being proportional to their mass. Objects like neutron stars and black holes, which have a lot of mass or energy, generate strong enough gravitational forces to warp spacetime in a very pronounced manner.

The warping of light rays around a black hole is schematically shown in Figure 1. Two light rays emanating from a star on the celestial sphere are deflected

around opposite sides of the black hole due to warping of spacetime. This will happen to all the stars on the celestial sphere near the black hole and this phenomena is known as *gravitational lensing*. The Einstein ring is an image of a point source that is on the celestial sphere, diametrically opposite to the camera. This point is the Caustic point, and the orange surface shows the locus of rays from this point converging at the camera. The Einstein ring is the intersection of these rays with the camera sky. For the star we will see two images in the camera sky, one inside the Einstein ring and the other outside it.

The principle of least action dictates that light rays follow geodesics in this curved spacetime. In order to generate the image of the curved spacetime due to the distortions produced in it by gravitational influence of phenomena like black holes, we must trace these geodesic paths. We derive the expressions for these geodesic paths, from principles of general relativity.

The notation used here is the index notation and Einstein summation convention used in general relativity. These have been explained in Appendix A. Interested readers can refer (Misner et al., 1973) (Hartle, 2003) (Collier, 2013) for more details.

Distance between two points in a spacetime is given by a metric. If the Minkowski metric is $\eta_{\alpha\beta}$, then proper time, τ can be written as

$$d\tau^2 = \eta_{\alpha\beta} d\xi^\alpha d\xi^\beta \quad (1)$$

where proper time is the time measured by an observer in their own rest frame. The Principle of Equivalence of Gravitation and Inertia states that at every spacetime point in an arbitrary gravitational field it is possible to choose a locally inertial coordinate system such that, within a sufficiently small region of the point in question, the laws of nature take the same form as in an accelerated Cartesian coordinate system in the absence of gravitation. Therefore, for a particle moving purely under the influence of gravitational forces, there is a freely falling coordinate system ξ^α in which its equation of motion is that of a straight line in spacetime (or equivalently is a geodesic of the spacetime). This can be written as

$$\frac{d^2\xi^\alpha}{d\tau^2} = 0 \quad (2)$$

Considering any other coordinate system x^μ , the freely falling coordinates ξ^α can be considered to be functions of x^μ , and Equation 2 can be re-written as

$$\frac{d}{d\tau} \left(\frac{\partial \xi^\alpha}{\partial x^\mu} \frac{dx^\mu}{d\tau} \right) = 0 \quad (3)$$

$$\frac{\partial \xi^\alpha}{\partial x^\mu} \frac{d^2x^\mu}{d\tau^2} + \frac{\partial^2 \xi^\alpha}{\partial x^\mu \partial x^\nu} \frac{dx^\mu}{d\tau} \frac{dx^\nu}{d\tau} = 0 \quad (4)$$

Multiplying this by $\frac{\partial x^\lambda}{\partial \xi^\alpha}$ and simplifying, gives us the equation of motion of the particle as

$$\frac{d^2x^\lambda}{d\tau^2} + \Gamma_{\mu\nu}^\lambda \frac{dx^\mu}{d\tau} \frac{dx^\nu}{d\tau} = 0 \quad (5)$$

where $\Gamma_{\mu\nu}^\lambda$ is the connection coefficient or Christoffel symbol, defined by

$$\Gamma_{\mu\nu}^\lambda = \frac{\partial x^\lambda}{\partial \xi^\alpha} \frac{\partial^2 \xi^\alpha}{\partial x^\mu \partial x^\nu} \quad (6)$$

Since light rays travel along null geodesics, i.e., paths on which proper time does not change, $d\tau = 0$, we replace $d\tau$ with another parameter ζ to get the geodesic equation that gives us the path of the light ray. In such a case, ζ represents the affine parameter that varies along the geodesic.

$$\frac{d^2x^\lambda}{d\zeta^2} + \Gamma_{\mu\nu}^\lambda \frac{dx^\mu}{d\zeta} \frac{dx^\nu}{d\zeta} = 0 \quad (7)$$

3.1 The Hamiltonian Formulation

The (Euler-Lagrange) geodesic equation derived in the previous section, though analytically perfect is not amenable to numerical simulation. For that purpose, we use a Hamiltonian formulation of the equation of motion. If we note that proper time can be written in an arbitrary coordinate system in terms of the metric tensor as

$$d\tau^2 = g_{\mu\nu} d\xi^\mu d\xi^\nu \quad (8)$$

where $g_{\mu\nu}$ is defined as

$$g_{\mu\nu} = \frac{\partial \xi^\alpha}{\partial x^\mu} \frac{\partial \xi^\beta}{\partial x^\nu} \eta_{\alpha\beta} \quad (9)$$

Now, a Hamiltonian can be constructed from the metric of the (pseudo-Riemannian) manifold representing the spacetime as

$$H(x^\alpha, p_\alpha) = \frac{1}{2} g^{\mu\nu}(x^\alpha) p_\mu p_\nu \quad (10)$$

Here $g^{\mu\nu}$ are the contravariant terms of the metric, x^α , is the coordinate of the photon travelling along the ray and p_α is the generalized momentum.

The equations of motion can now be written as

$$\frac{dx^\alpha}{d\zeta} = \frac{\partial H}{\partial p_\alpha} = g^{\alpha\nu} p_\nu \quad (11)$$

$$\frac{dp_\alpha}{d\zeta} = -\frac{\partial H}{\partial x^\alpha} = -\frac{1}{2} \frac{\partial g^{\mu\nu}}{\partial x^\alpha} p_\mu p_\nu \quad (12)$$

It can be proved that these equations are together equivalent to Equation 7. This form makes

it easy for us to write 6 first order differential equations for the 6 variables of motion (three coordinates, three momenta), which can then be integrated to get the ray path. We can solve these equations for any given spacetime metric. In the next section, we present the solutions for the Schwarzschild, Kerr and Ellis metrics, which describe spacetime around a Schwarzschild black hole, Kerr black hole and Ellis worm hole respectively. In all the metric equations discussed below, we have assumed light speed $c = 1$.

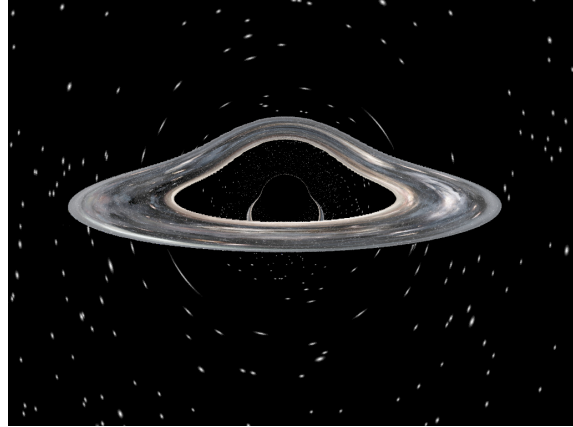


Figure 2: Here we can see an accretion disk rendered around a Schwarzschild black hole rendered using our ray tracer.

3.1.1 The Schwarzschild Metric Solution

The Schwarzschild solution was the first exact solution to the Einstein field equations (Schwarzschild, 1916). It describes a static, spherically symmetric, gravitational field in the empty region of spacetime near a massive spherical object. In isotropic coordinates, the metric is given by

$$ds^2 = \left(\frac{1 - \frac{r_s}{4R}}{1 + \frac{r_s}{4R}} \right)^2 dt^2 - \left(1 + \frac{r_s}{4R} \right)^4 (dx^2 + dy^2 + dz^2) \quad (13)$$

Here r_s is the Schwarzschild radius, $r_s = 2GM$, where G is the gravitational constant and M is the mass of the body. R is the radius of the spherical body. The contravariant metric tensor can thus be written as

$$g_{\mu\nu} = diag \left(\left(\frac{1 - \frac{r_s}{4R}}{1 + \frac{r_s}{4R}} \right)^2, - \left(1 + \frac{r_s}{4R} \right)^4, - \left(1 + \frac{r_s}{4R} \right)^4, - \left(1 + \frac{r_s}{4R} \right)^4 \right) \quad (14)$$

Now, for $\alpha = 0$, $x^\alpha \equiv t$, the equations of motion, Equations 11 and 12 give

$$\frac{dt}{d\zeta} = \left(\frac{1 + \frac{r_s}{4R}}{1 - \frac{r_s}{4R}} \right)^2 p_t \quad (15)$$

$$\frac{dp_t}{d\zeta} = 0 \quad (16)$$

The second of these equations implies that p_t is a constant, and thus we can conveniently choose $p_t = -1$ to get

$$\frac{d\zeta}{dt} = - \left(\frac{1 - \frac{r_s}{4R}}{1 + \frac{r_s}{4R}} \right)^2 \quad (17)$$

We similarly write for $\alpha = 1, 2, 3$ the equations

$$\frac{dx^\alpha}{d\zeta} = - \left(1 + \frac{r_s}{4R} \right)^{-4} p_\alpha \quad (18)$$

$$\frac{dp_\alpha}{d\zeta} = \frac{1}{2R^3} \left(\frac{(p_x^2 + p_y^2 + p_z^2)}{\left(1 + \frac{r_s}{4R} \right)^5} + \frac{\left(1 + \frac{r_s}{4R} \right)}{\left(1 - \frac{r_s}{4R} \right)^3} \right) r_s x^\alpha \quad (19)$$

Using the equation for $\frac{d\zeta}{dt}$, we can obtain

$$\frac{dx^\alpha}{dt} = \left(1 + \frac{r_s}{4R} \right)^{-6} \left(1 - \frac{r_s}{4R} \right)^2 p^\alpha \quad (20)$$

$$\begin{aligned} \frac{dp_\alpha}{dt} &= - \frac{1}{2R^3} \left((p_x^2 + p_y^2 + p_z^2) \frac{\left(1 - \frac{r_s}{4R} \right)^2}{\left(1 + \frac{r_s}{4R} \right)^7} \right. \\ &\quad \left. + \left(1 - \left(\frac{r_s}{4R} \right)^2 \right)^{-1} \right) r_s x^\alpha \end{aligned} \quad (21)$$

Since there is no cross dependence amongst coordinate evaluations, we can normalize p_α , and it does not make any difference to integration, except changing the functions by a scale factor. It just results in time re-scaling, and does not affect us for a static visualization.

We integrate Equations 20 and 21, to get the path of the light ray in a spacetime near a Schwarzschild black hole. An example of a scene with a Schwarzschild black hole can be seen in Figure 7. Figure 2 shows a realistic looking accretion disk where the warping of spacetime bends the disk and makes it appear around the Schwarzschild black hole.

The solution for other metrics can be similarly derived, and therefore we can handle any arbitrary metric representing a spacetime.

3.1.2 The Kerr Metric Solution

The Kerr metric describes the geometry of empty spacetime around a rotating, uncharged, axially-symmetric black hole. In spherical coordinates the

Kerr metric (Chandrasekhar, 2002) for a mass M rotating with angular momentum J is given as

$$ds^2 = \rho^2 \frac{\Delta}{\Sigma^2} dt^2 - \frac{\Sigma^2}{\rho^2} \left(d\phi - \frac{2aMr}{\Sigma^2} dt \right)^2 \sin^2 \theta \quad (22)$$

$$- \frac{\rho^2}{\Delta} dr^2 - \rho^2 d\theta^2$$

where $a = J/M$, $\rho^2 = r^2 + a^2 \cos^2 \theta$, $\Delta = r^2 - 2Mr + a^2$, $\delta = \sin^2 \theta$, $\Sigma^2 = (r^2 + a^2)^2 - a^2 \Delta \delta$.

Here, the contravariant metric tensor is given by

$$g_{\mu\nu} = \begin{bmatrix} 1 - \frac{2Mr}{\rho^2} & 0 & 0 & \frac{2aMr \sin^2 \theta}{\rho^2} \\ 0 & -\frac{\rho^2}{\Delta} & 0 & 0 \\ 0 & 0 & -\rho^2 & 0 \\ \frac{2aMr \sin^2 \theta}{\rho^2} & 0 & 0 & -\left[(r^2 + a^2) + \frac{2a^2 Mr \sin^2 \theta}{\rho^2} \right] \sin^2 \theta \end{bmatrix} \quad (23)$$

Evaluating the Hamiltonian, as explained in Section 3.1, we get the rate of change of position with time as

$$\frac{dr}{dt} = \frac{\Delta}{\rho^2} \left(\frac{d\zeta}{dt} \right) p_r \quad (24)$$

$$\frac{d\theta}{dt} = \frac{1}{\rho^2} \left(\frac{d\zeta}{dt} \right) p_\theta \quad (25)$$

$$\frac{d\phi}{dt} = \frac{p_t \frac{2aMr \sin^2 \theta}{\rho^2} + p_\phi \left(1 - \frac{2Mr}{\rho^2} \right)}{p_t \left[(r^2 + a^2) + \frac{2aMr \sin^2 \theta}{\rho^2} \right] \sin^2 \theta - p_\phi \frac{2aMr \sin^2 \theta}{\rho^2}} \quad (26)$$

where $\frac{d\zeta}{dt}$ is defined as

$$\frac{d\zeta}{dt} = \frac{\left(1 - \frac{2Mr}{\rho^2} \right) \left[(r^2 + a^2) + \frac{2aMr \sin^2 \theta}{\rho^2} \right] \sin^2 \theta + \left(\frac{2aMr \sin^2 \theta}{\rho^2} \right)^2}{p_t \left[(r^2 + a^2) + \frac{2aMr \sin^2 \theta}{\rho^2} \right] \sin^2 \theta - p_\phi \frac{2aMr \sin^2 \theta}{\rho^2}} \quad (27)$$

The rate of change of momentum with time is similarly obtained as

$$\begin{aligned} \frac{dp_r}{dt} &= M \left(\frac{-r^2 + a^2 \sin^2 \theta}{\rho^4} \right) i \\ &\quad - 2aM \sin^2 \theta \left(\frac{-r^2 + a^2 \sin^2 \theta}{\rho^4} \right) \dot{\phi} \\ &\quad + \frac{\Delta r - \rho^2(r - M)}{\Delta^2} \frac{i^2}{t} + r \frac{\dot{\theta}^2}{t} \\ &\quad + \left[r + a^2 M \sin^2 \theta \left(\frac{-r^2 + a^2 \sin^2 \theta}{\rho^4} \right) \right] \sin^2 \theta \frac{\dot{\phi}^2}{t} \end{aligned} \quad (28)$$

$$\begin{aligned} \frac{dp_\theta}{dt} &= \frac{2a^2Mr\sin\theta\cos\theta}{\rho^4}\dot{t} \\ &- \frac{4aMr(\rho^2\sin\theta\cos\theta + a^2\sin^3\theta\cos\theta)}{\rho^4}\dot{\phi} \\ &- \frac{a^2\sin\theta\cos\theta\dot{r}^2}{\Delta}\dot{t} - a^2\sin\theta\cos\theta\frac{\dot{\theta}^2}{\dot{t}} \\ &+ [(r^2 + a^2)\sin\theta\cos\theta]\frac{\dot{\phi}^2}{\dot{t}} \\ &+ \left[\frac{2a^2Mr}{\rho^4}(2\rho^2\sin^3\theta\cos\theta + a^2\sin^5\theta\cos\theta) \right] \frac{\dot{\phi}^2}{\dot{t}} \end{aligned} \quad (29)$$

$$\frac{dp_t}{dt} = 0 \quad (30)$$

$$\frac{dp_\phi}{dt} = 0 \quad (31)$$

where $\dot{x} = \frac{dx}{d\tau}$ for any variable x . These equations are stable for numerical integration, except at the poles $\theta = 0$ and $\theta = \pi$. In this formulation, p_t and p_ϕ are conserved along the ray. The ray has two more conserved quantities as explained below. These are the axial angular momentum, B_1 and total angular momentum, B_2 . We use these two quantities to track the stability of the numerical integration during path tracing.

$$\begin{aligned} B_1 &= -\frac{p_\phi}{p_t} \\ B_2 &= \frac{p_\theta^2 + \cos^2\theta \left(\frac{p_\phi^2}{\sin^2\theta} - a^2 \right)}{p_t^2} \end{aligned} \quad (32)$$

One can verify that the solution of Kerr black hole metric reduces to the solution of Schwarzschild black hole metric when $a = 0$. Thus, as the value of a , i.e., angular momentum per unit mass increases, the rotational energy present in the black holes increases. Now as per Einstein's general theory of relativity, this rotational energy term contributes to the mass of the black hole. Thus the effective mass of a Kerr black hole is more than its original/irreducible mass. It can be proved (Chandrasekhar, 2002) that the total mass equivalent M of the black hole including its rotational energy and its irreducible mass M_{irr} are related by

$$M = 2\sqrt{\frac{M_{irr}^4}{4M_{irr}^2 - \frac{a^2}{G^2}}} \quad (33)$$

As a result when $\frac{a}{M}$ varies from 0.0 to 1.0 the equivalent mass of Kerr black hole varies from $M = M_{irr}$ to $M = \sqrt{2}M_{irr}$. So the spacetime distortion is greater for the Kerr black hole which has a higher $\frac{a}{M}$ ratio which in turn implies more rotational energy. We

demonstrate the variation of this distortion in Figure 10.

3.1.3 The Ellis Metric Solution

The Einstein field equations have valid solutions that contain wormholes. A wormhole is like a tunnel between two points in spacetime. One of the earliest known traversable wormholes is the Ellis wormhole. The Ellis wormhole metric (Ellis, 1973), in spherical coordinates, is given by

$$ds^2 = dt^2 - dl^2 - r^2(d\theta^2 + \sin^2\theta d\phi^2) \quad (34)$$

where r is a function of the coordinate l , defined as $r = \sqrt{\rho^2 + l^2}$ and ρ is a constant.

The Hamiltonian in this case is as follows

$$H = \frac{1}{2} \left[p_t^2 - p_l^2 - \frac{p_\theta^2}{r^2} - \frac{p_\phi^2}{r^2 \sin^2\theta} \right] \quad (35)$$

Since H is independent of the time parameter t and ϕ , p_t and p_ϕ are conserved along the ray. The total angular momentum is also conserved, as the wormhole is spherical and is given by $B = p_\theta^2 + \frac{p_\phi^2}{\sin^2\theta}$. Evaluating the Hamiltonian, we obtain the equations for the rate of change of position and momentum along time. Let

$$\frac{dt}{d\zeta} = p_t = -1 \quad (36)$$

which shows that $\zeta = t$, up to a constant, and replacing ζ by t gives us five equations for $l, \theta, \phi, p_l, p_\theta$ as functions of time t , along the ray.

$$\frac{dl}{dt} = p_l, \quad \frac{d\theta}{dt} = \frac{p_\theta}{r^2} \quad (37)$$

$$\frac{d\phi}{dt} = \frac{p_\phi}{r^2 \sin^2\theta}, \quad \frac{dp_l}{dt} = B^2 \frac{dr/dl}{r^3}, \quad \frac{dp_\theta}{dt} = \frac{p_\phi^2}{r^2} \frac{\cos\theta}{\sin^3\theta} \quad (38)$$

These equations are also stable for numerical integration, except at the poles $\theta = 0$ and $\theta = \pi$. Integrating these gives us the geodesics that the light rays follow in the spacetime around an Ellis wormhole.

4 IMPLEMENTING RAY-OBJECT INTERACTIONS IN CURVED SPACETIME

We use a Monte Carlo path tracer to render curved spacetime for visualization. An important step in path tracing is calculating the intersection of the sample ray with the geometry in the scene. For rays that

travel in a straight line, and hence can be represented by a one parameter equation, it is easy to find closed form expressions for intersection with simple objects such as spheres, cylinders, cones and cuboids. Even complicated geometry can be represented with triangle meshes and a ray-triangle intersection is not hard to compute.

For warped spacetime, we have to integrate the ray in time, and even for the simplest of objects, it is often not possible to find an analytic solution for the intersection. A numerical solution also seems difficult when we want our scheme to be compatible with a potentially arbitrary set of metrics and geometrical objects. We find an intersection by integrating the rays one step along the null geodesic at a time, and we keep decreasing this step size as we approach an object until we converge to an intersection within machine precision.

Therefore, in the overall Monte Carlo path tracing loop we replace the instantaneous ray directions by those given by the solution to the null geodesic, as derived in the previous section, and we step along this direction as explained in Algorithm 1

Algorithm 1 Path tracing & ray-object intersection in curved space

```

1: while number of iterations < MAXITER do
2:   Let the current position along the Ray be  $x^\alpha$ .
3:   Let current time be  $t$  and current time
   step be  $dt$ .
4:   Move forward from this position by integrating
   the geodesic, to a new position along the ray  $y^\alpha$ .
5:   Let  $\hat{n}$  be unit object surface normal.
6:   if  $x^\alpha \cdot \hat{n} \neq y^\alpha \cdot \hat{n}$  then
7:     Find perpendicular distance,  $\delta$ , to
     the object surface from current point.
8:     if  $\delta < \epsilon$  then
9:       return radiance and normal at
         point on surface.
10:    else
11:      Reset current position on ray to  $x^\alpha$ .
12:       $dt = dt/2$ .
13:    end if
14:  end if
15: end while
16: return no intersection (radiance returned is zero).
  
```

In our implementation, ϵ is defined to $1e-10$. We use a Runge-Kutta Order 4 integrator for our path tracer. Depending on scene complexity, the maximum number of iterations (MAXITER) for our experiments varies from 100 to 4000 and our starting time step size, dt , varies from 10.0 to 0.5. Specifically,

for generating renders with the Ellis wormhole metric and Kerr black hole metric, we monitor the constants for a geodesic, p_ϕ , p_θ and B, B_1, B_2 . These constants are monitored through the integration and if they deviate from the expected values by more than a specified threshold, we halve the time step for the integration. If they deviate further than a stricter threshold, we simply terminate the integration for that ray path (geodesic), and mark the corresponding pixel as erroneous. We later process these erroneous pixels through a local smoothing step to improve the image in the error region. The results of this error correction can be seen in Section 5.

We also sample our rays on a jittered grid to get an anti-aliased image. On the CPU, we use OpenMP to speed up the outermost ray tracing loop by using `omp parallel`. Apart from that, the only other point of note was that to render a image of size 1024×768 we had a global work size of 1024×768 , so one work item per pixel is used which computes the intensity at that pixel. Thus, the memory available on the graphics card is a restriction in such a case.

5 RESULTS AND DISCUSSION

Here we present extensive demos of our spacetime renderer.

5.1 Validation Results

A renderer that claims to render curved spacetime must also work correctly when spacetime is not curved, i.e., the trivial solution of the Einstein field equations. So we used a Minkowski metric in our path integration algorithm, and rendered the Cornell room. The output exactly matches the expected output of a normal Monte Carlo path tracer that works in flat spacetime. This is shown in Figure 3.

In order to validate the path tracing in curved spacetime, we render known models of cosmological phenomena. We show our simulation of an Einstein ring, as visualized using our renderer in Figure 4. We further show our render of gravitational lensing, and distinct multiple images of a star being produced due to the phenomena in Figure 5. We can see that the images of the stars produced by gravitational lensing are stretched. This is because of the way spacetime warps around the black hole and the fact that light paths that start out together spread (or squash) during the process. If for visual aesthetic reasons we want stars to only appear as point sources, even in the distorted starfield, it can be achieved by tracing light ray

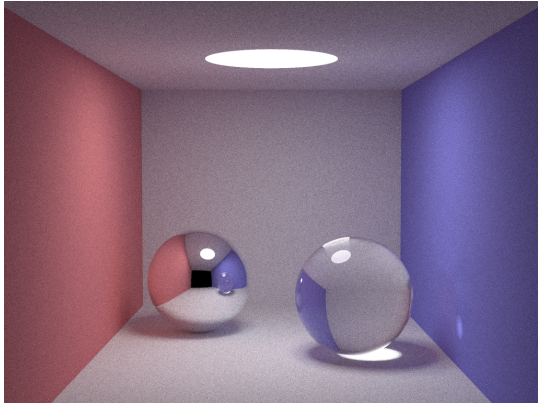


Figure 3: The image of a Cornell box generated by our code in a flat spacetime, where all rays travel in a straight line.

bundles, instead of single light rays, and then computing the effect of spacetime distortion on the cross sections of these light ray bundles.

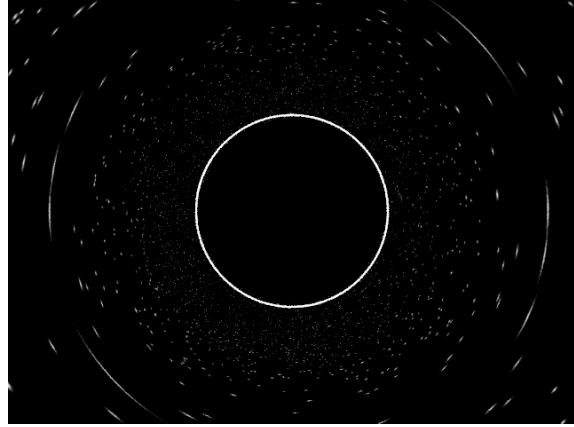


Figure 4: This Einstein ring is produced by placing a light source behind a black hole diametrically opposite the camera, at the caustic point. We cannot directly see the light source, but the rays can curve around the black hole to reach us. The warping of the surrounding starfield follows the predicted pattern.

We also show the accretion disk around a stationary and rotating black hole. Figure 6 shows a thin accretion disk with a color swatch texture on it being warped by two different black holes. We can look at the color of the paint swatch at a location on the disk and see that parts of the disk are visible more than once around the black hole. The warping of spacetime bends the disk and makes it appear around the black holes. Moreover, the colour patches on the accretion disk of Kerr black hole appear to be more warped compared to the Schwarzschild black hole. This is because of the rotational drag present in the Kerr black hole. The $\frac{a}{M}$ ratio of the Kerr black hole is 0.9.

Thus we see that our renderer correctly produces

visualizations of expected cosmological phenomena as is predicted by the theory of general relativity. We next demonstrate our results on everyday scenes, rendered in curved spacetime.

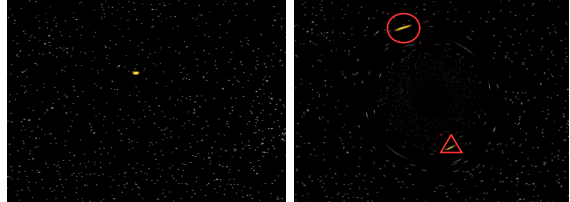


Figure 5: Here we can see a starfield warped by a Schwarzschild black hole. Distinct multiple images of the same stars can be seen. To illustrate this we have marked a star in bright yellow in the undistorted starfield image seen on the left. We can see two images of the bright star in the starfield warped by the black hole, in the right image. The primary image of the star is seen on the top, marked by the red circle and the secondary image of the star is seen on the bottom, marked by the red triangle.

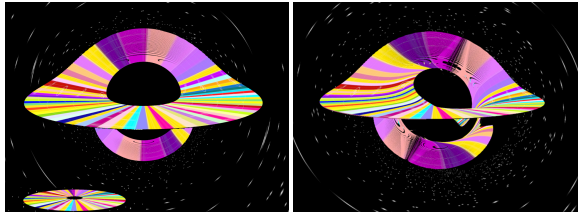


Figure 6: Here we see an accretion disk around a Schwarzschild black hole on the left and Kerr black hole on the right. The undistorted paint swatch texture used on the disk can be seen on the lower left corner. The black hole warps spacetime and portions of the same paint swatch appears both below and above the black hole. This is because the light rays from the disk are bent by the black hole along multiple paths and form repeated images. Moreover, in the rotating black hole straight radial lines on the texture appear curved due to the more pronounced curvature of spacetime.

5.2 Everyday Scenes Around a Schwarzschild and a Kerr Black Hole

The everyday scene we choose here is the Cornell room scene shown in Figure 3. We can see a number of global illumination phenomena in this room, including multiple reflections and refractions, caustics, area lights and soft shadows, and diffuse to diffuse light transfer. We render a Schwarzschild and multiple Kerr black holes with different $\frac{a}{M}$ ratio.

In Figure 7 we show a Schwarzschild black hole open in the middle of the room. Notice the bending of the geometry of the room in the warped space-

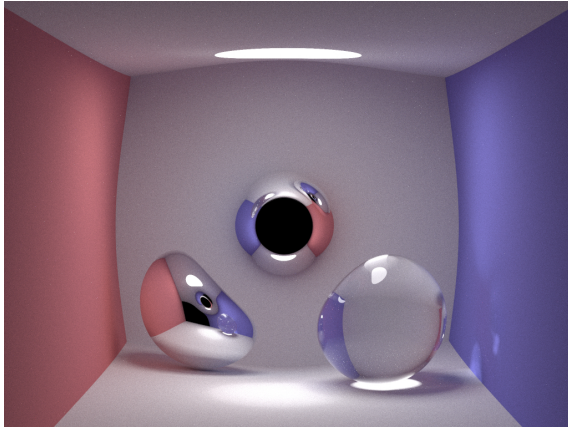


Figure 7: The image illustrates a stationary Schwarzschild black hole of radius 5 units placed right in the center of the Cornell room.

time around the black hole. The black hole has a event horizon of radius 5 units. The black hole is in the middle of the room, even in depth, not on the back wall. In Figure 8, a Schwarzschild black hole

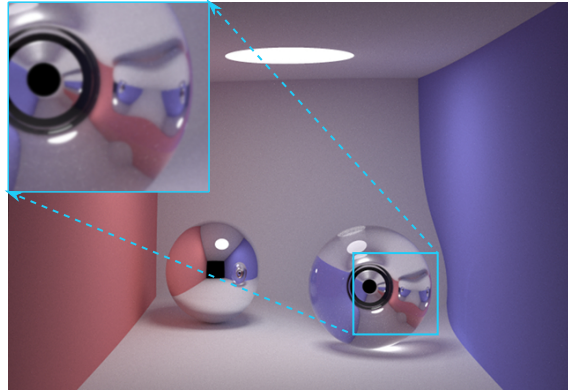


Figure 8: We place a Schwarzschild black hole inside the refractive glass sphere. We can clearly see the images of the walls being sucked in towards the center. In the zoomed up inset image, we can see two images of the room on the right hand side, both being curved and refracted from different regions.

of Schwarzschild radius 1.6 units sits inside a refractive ball of refractive index 1.5 which has a radius of 16 units. The image is formed because of a combination of the lensing effect by the black hole and the refraction from the ball’s surface. We can see rings of darkness in the regions where the black hole directs light rays at an angle such that they don’t refract out of the ball, while the lit rings are regions where the light refracts towards us after being curved from the black holes. Very notable is the dual image of the refractive ball against the blue background on the right hand side of the ball. Those rays reflect off the reflecting ball on the left and then enter again into the

refractive ball, where the black hole curves different rays from the same part of the scene into different regions of the image, thus allowing us to see multiple images of the same source. Similar effect can be seen for a Kerr black hole.



Figure 9: The image shows a rotating Kerr black hole in a starfield. Warped spacetime can be clearly seen here along with phenomena like gravitational lensing.

Figure 9 illustrates a warped starfield in presence of a rotating Kerr black hole with a/M ratio of 0.9. In Figure 10 we show Kerr black holes with different a/M ratios, in the middle of the room. The bending of the geometry of the room in the warped spacetime around the black hole is more pronounced as the ratio a/M increases. All the black holes have an event horizon of radius 5 units. Same as before all the black holes are in the middle of the room (even in depth) and not on the back wall.

Gravitational lensing, as explained in Section 3 is seen with streak lines formed by images of stars in the presence of a moving observer (James et al., 2015a). We show lensing due to two kinds on black holes in Figure 11, where we have colored a few lines on the grid so that we can track where the exact primary and secondary images are formed.

5.3 Everyday Scenes Around an Ellis Wormhole

We now present our renders for visualizations around an Ellis wormhole. A wormhole connects two different regions in spacetime, so light rays can travel through the wormhole from one region to another. In our final sequence of renders, we show a view from a wormhole, with one end inside the room and the other end in outer space in Figure 12. A satellite (shown as the green cylinder) orbits the earth in outer space.

In Figure 13, two images each of both the earth and the satellite can be seen as crescent shaped disks

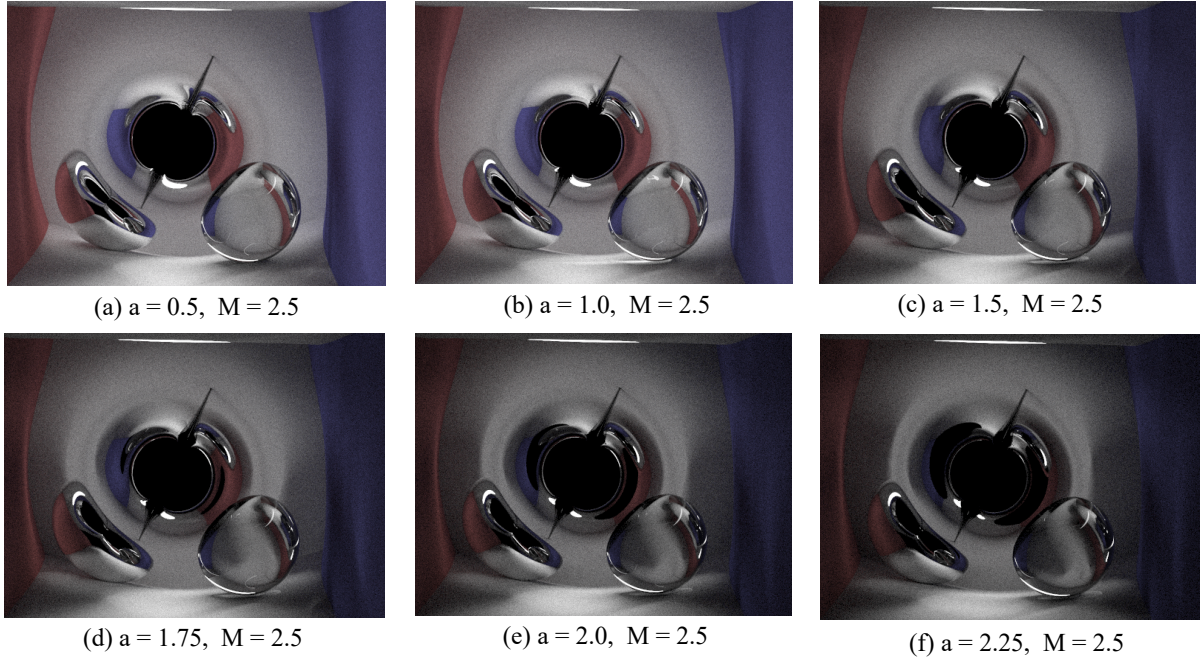


Figure 10: These are Kerr black holes of radius 5 units and varying a/M ratios placed right in the center of the Cornell room. In the left, the spacetime distortion is less as the black hole has a lower a/M ratio compared to right one. In the right image the distortion is so high that the light is not able to reach everywhere in the scene, thus giving the image a darker appearance.

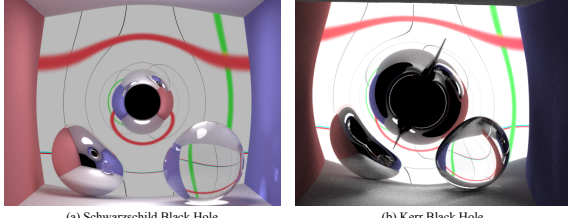


Figure 11: Here we show another example of gravitational lensing rendered by our path tracer for two kinds of black holes. A rectangular grid has been mapped on the back wall of the room, on which we have coloured one horizontal line red and one vertical line green. The red band on top of the black hole is the primary image of the red line, whereas the curved red line at the bottom that starts and end at the black hole, is the secondary image of the red line. Similarly, the green line to the right is the primary image, and to the left is the secondary image. Moreover for Kerr black hole the spacetime distortion is more as evident from the curvature of lines.

in outer space when looked at from the side of the wormhole that is inside the room. Similarly the room can be seen when looked at from the side of the wormhole that is in space as shown in Figure 12. This demonstrates that rays of light do correctly bend from one spacetime region to another, via the wormhole as is expected.

The view of the room appears dim when seen through the wormhole end in outer space as in the Monte Carlo path tracer very few ray samples make

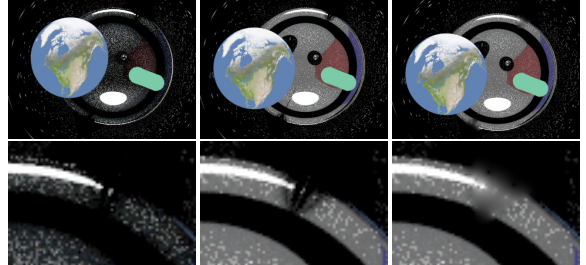


Figure 12: The top row shows the view from one end of the Ellis wormhole that is in outer space. The left image is generated with normal Monte Carlo path tracing, the middle with Bidirectional path tracing and the final image has additional local smoothing applied to the regions where the wormhole metric is not numerically stable. The bottom row shows detail of what happens in one of the regions of numerical instability on the top rim of the wormhole with the three respective rendering methods used in the top row.

it through the wormhole back to the light source in the room. This can be corrected by bidirectional path tracing in curved spacetime, caching the illumination from the light source to the walls in the room in light maps stored on the room walls.

The wormhole geodesic solution is not well behaved near the poles, as is explained earlier. We terminate the rays near the poles to avoid numerical instability, which causes the black protruding error envelopes to be seen coming out of the wormhole. The black error regions can be filled by propagating the

intensity information from nearby non-error pixels to the pixels that are in the error envelop. This is like local smoothing at these pixels. We can also use more complex reconstruction kernels to cover up the error regions, if desired. We compare the renders gener-

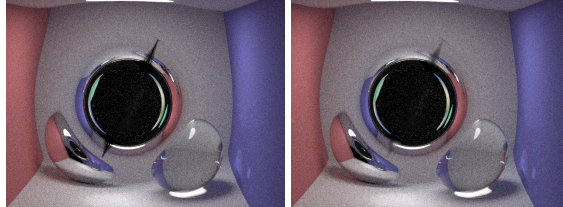


Figure 13: These show the view through the end of an Ellis wormhole that is inside the room. The wormhole also exerts strong gravitational forces on its surrounding spacetime and distorts the geometry of the room. The earth and the satellite from the other side of the wormhole can be seen through it as crescent shaped disks. The left image has pronounced error regions at diametrically opposite sides of the wormhole’s mouth which are seen as black protrusions. The right image has been locally smoothed by our renderer in the error regions.

ated by our Monte Carlo path tracer, our Bidirectional path tracer and our Bidirectional path tracer with local smoothing in error regions in Figure 12 that shows the view from the end that is in outer space. We can see that the view of the room in the wormhole improves a lot with bidirectional path tracing, and the error regions are significantly reduced due to the smoothing. Figure 13 shows the view from the room side of the wormhole.

5.4 Computational Complexity

All the images are rendered on a 2.4 GHz Intel i5 CPU using 4 threads with 1000 samples per pixel. Here we report the timing to render an image of size 1024×768 of a Cornell box, containing a mirror and a glass sphere, by placing a black or worm hole of size 5 units in the middle of the box. With Schwarzschild black hole it takes around 80 minutes to render. Rendering time with Kerr black hole ranges from 100 minutes ($a/M = 0.1$) to 200 minutes ($a/M = 0.9$). Due to bidirectional ray tracing and error smoothing the Ellis wormhole takes longer, nearly 250 minutes.

5.5 Limitations of Our Renderer

Our results are limited somewhat in the complexity of our scenes, but we do believe we demonstrate the full range of capabilities that our prototype system currently has. One major limitation of our renderer is that it cannot visualize dynamic scenes in curved spacetimes, as the animation trajectories of such movement

would also curve (in all four dimensions) that we do not presently compute. Also of interest may be setting up space partitioning schemes in curved spacetime to accelerate such renders.

Also, errors similar to the Ellis wormhole appear in the images with a Kerr black hole too. We can apply the same correction to those images as well, which we have not yet done in the current implementation.

6 CONCLUSION

We present a method to render warped spacetime. We do this by tracing rays along the null geodesic for the spacetime, where the spacetime geometry is described by its metric. We present a generic ray path integration scheme that allows us to trace these rays once the metric has been specified, and the desired geodesic equations have been derived. This scheme allows us to handle ray-object intersections and illumination phenomena while rendering curved spacetime. We show a number of results to validate the output that our renderer is producing, on standard scenes and cosmological phenomena that have been previously visualized. Then we render everyday scenes at terrestrial scales in warped spacetime, around black holes and wormholes. We believe that these visualizations give us a unique understanding of spacetime in everyday and familiar settings, making it of intrinsic pedagogic value. This rendering method is also very easy to integrate in any path tracer, and therefore in existing production pipelines. This also makes it ideal for producing VFX that are better and more accurately modelled with real physical basis.

REFERENCES

- Bauböck, M., Psaltis, D., Özel, F., and Johannsen, T. (2012). A Ray-tracing Algorithm for Spinning Compact Object Spacetimes with Arbitrary Quadrupole Moments. II. Neutron Stars. *The Astrophysical Journal*, 753(2):175.
- Chan, C.-k., Psaltis, D., and Ozel, F. (2013). GRay: a Massively Parallel GPU-Based Code for Ray Tracing in Relativistic Spacetimes. *The Astrophysical Journal*, 777:13.
- Chandrasekhar, S. (2002). *The mathematical theory of black holes*. Oxford classic texts in the physical sciences. Oxford Univ. Press, Oxford.
- Collier, P. (2013). *A Most Incomprehensible Thing: Notes Towards a Very Gentle Introduction to the Mathematics of Relativity*. Peter Collier.
- Ellis, H. G. (1973). Ether flow through a drainhole - a particle model in general relativity. *J. Math. Phys.*, 14:104–118.

- Fukue, J. and Yokoyama, T. (1988). Color photographs of an accretion disk around a black hole. *Publications of the Astronomical Society of Japan*, 40(1):15–24.
- Hamilton, A. (2008). Black hole flight simulator. [Online; accessed 01-December-2019].
- Hartle, J. B. (2003). *Gravity: An Introduction to Einstein's General Relativity*. Benjamin Cummings, illustrate edition.
- James, O., Tunzelmann, E. v., Franklin, P., and Thorne, K. S. (2015a). Gravitational lensing by spinning black holes in astrophysics, and in the movie interstellar. *Classical and Quantum Gravity*, 32(6):065001.
- James, O., von Tunzelmann, E., Franklin, P., and Thorne, K. S. (2015b). Visualizing interstellar's wormhole. *American Journal of Physics*, 83(6):486–499.
- Kerr, R. P. (1963). Gravitational field of a spinning mass as an example of algebraically special metrics. *Physical review letters*, 11(5):237.
- Kuchelmeister, D., Muller, T., Ament, M., Wunner, G., and Weiskopf, D. (2012). Gpu-based four-dimensional general-relativistic ray tracing. *Computer Physics Communications*, 183(10):2282 – 2290.
- Luminet, J. P. (1979). Image of a spherical black hole with thin accretion disk. *Astronomy and Astrophysics*, 75:228–235.
- Marck, J.-A. (1996). Shortcut method of solution of geodesic equations for Schwarzschild black hole. *Classical and Quantum Gravity*, 13:393–402.
- Misner, C., John Archibald Wheeler, C., Misner, U., Thorne, K., Wheeler, J., Thorne, U., Freeman, W., and Company (1973). *Gravitation*. Number pt. 3 in Gravitation. W. H. Freeman.
- Morris, M. S. and Thorne, K. S. (1988). Wormholes in space-time and their use for interstellar travel: A tool for teaching general relativity. *Am. J. Phys.*, 56:395–412.
- Müller, T. (2014). Geovis—relativistic ray tracing in four-dimensional spacetimes. *Computer Physics Communications*, 185(8):2301 – 2308.
- Müller, T. and Boblest, S. (2011). Visualizing circular motion around a schwarzschild black hole. *American Journal of Physics*, 79(1):63–73.
- Müller, T., Grottel, S., and Weiskopf, D. (2010). Special relativistic visualization by local ray tracing. *IEEE Transactions on Visualization and Computer Graphics*, 16(6):1243–1250.
- Psaltis, D. and Johannsen, T. (2012). A Ray-tracing Algorithm for Spinning Compact Object Spacetimes with Arbitrary Quadrupole Moments. I. Quasi-Kerr Black Holes. *The Astrophysical Journal*, 745(1):1.
- Schwarzschild, K. (1916). Über das Gravitationsfeld eines Massenpunktes nach der Einsteinschen Theorie. *Sitzungsberichte der Königlich Preußischen Akademie der Wissenschaften (Berlin)*, 1916, Seite 189-196.
- Thorne, K. (2015). *The science of interstellar*. W. W. Norton, New York, NY.
- Viergutz, S. U. (1993). Image generation in Kerr geometry. I. Analytical investigations on the stationary emitter-observer problem. *Astronomy and Astrophysics*, 272:355.
- Vincent, F. H., Paumard, T., Gourgoulhon, E., and Perrin, G. (2011). GYOTO: a new general relativistic ray-tracing code. *Classical and Quantum Gravity*, 28(22):225011.
- Weiskopf, D., Schafhitzel, T., and Ertl, T. (2004). Gpu-based nonlinear ray tracing. *Comput. Graph. Forum*, 23:625–634.

APPENDIX

Index Notation and the Einstein Summation Convention

In Cartesian coordinates, A vector \mathbf{V} consists of a product of its components (V_x, V_y, V_z) and its basis vectors $(\hat{e}_x, \hat{e}_y, \hat{e}_z)$

$$\mathbf{V} = V_x \hat{e}_x + V_y \hat{e}_y + V_z \hat{e}_z \quad (39)$$

In index notation, this can be concisely written as $\mathbf{V} = V_i e_i$. Contravariant vectors (and tensors) are denoted by an upper index (e.g. V^α), while covariant vectors are denoted by a lower index (e.g. V_α).

Spacetime has four coordinates. It is convention to use Greek indices ($\alpha, \beta, \gamma \dots$) to represent them, the index taking values 0, 1, 2, 3 where 0 refers to the time coordinate and 1, 2, 3 to the three spatial coordinates.

In Einstein summation convention when an index occurs twice in the same expression, it means that the expression is implicitly summed over all possible values for that index. For Cartesian vectors, the scalar product $\mathbf{A} \cdot \mathbf{B} = A_x B_x + A_y B_y + A_z B_z$ can be written in this convention simply as $A_i B_i$. Tensors can have more than one index. Two tensor $X_{\mu\nu}$ and Y^ν being summed over $\nu = 0, 1, 2, 3$ can be written as $X_{\mu\nu} Y^\nu$. The index ν here is known as a dummy index and the μ as a free index.

It should be noted that free indices only appear as either subscript or superscript, never as both and they must occur exactly once in each term. Dummy indices appear twice in a term, once as subscript and once as superscript in general four vectors and tensors.

Index labels are themselves not important, and subject to rules for dummy and free indices. They can also be arbitrarily renamed in expressions, without loss of meaning.